

## Near-field characterization of surface plasmon polaritons on a nanofabricated transmission structure

Aleksandra Sierant <sup>\*</sup>, Benedykt R. Jany, and Tomasz Kawalec

*Marian Smoluchowski Institute of Physics, Jagiellonian University in Krakow, Lojasiewicza 11, 30-348 Kraków, Poland*



(Received 2 February 2021; revised 14 April 2021; accepted 15 April 2021; published 30 April 2021)

The tailoring of plasmonic near fields is central to the field of nanophotonics. Detailed knowledge of the field distribution is crucial for design and fabrication of plasmonic sensors, detectors, photovoltaics, plasmon-based circuits, nanomanipulators, electro-optic plasmonic modulators, and atomic devices. We report on a quantitative comparison between near-field observation and numerical calculations, considering the intensity distribution for transverse magnetic (TM) and transverse electric (TE) polarizations, which are necessary for the construction of devices in all these areas. We present the near-field scanning microscopy (NSOM) results of surface plasmon polaritons (SPPs), excited by linearly polarized illumination on a gold, nanofabricated transmission grating. The optimization process is performed for infrared light for applications in cold-atom trapping and plasmonic sensing. We show the *in situ* processes of buildup and propagation of SPPs and confirm that the out of plane component of the electric field is not coupled to the aperture-type NSOM probe.

DOI: [10.1103/PhysRevB.103.165433](https://doi.org/10.1103/PhysRevB.103.165433)

### I. INTRODUCTION

Near-field scanning microscopy (NSOM) is a well-known imaging technique for optical near-field examination. Nowadays, it is one of the most powerful imaging tools thanks to a wide range of probe types and achievable subwavelength resolutions [1–3]. The technique provides a unique opportunity to investigate physical processes such as extraordinary optical transmission [4], light propagation in photonic crystal waveguides [5], and dynamics of plasmonic nanoantennas [6,7]. Knowledge of the distribution of the near field allows for the design of a number of devices, e.g., nanomanipulators [8,9], sensors based on surface enhanced Raman spectroscopy [10], plasmonic sensors [11], surface plasmon-based circuits [12,13], electro-optic plasmonic modulators [14], and chip-scale atomic devices [15]. Understanding of near fields is necessary for the construction of structured optical potentials for cold atoms, e.g., atom mirrors and plasmonic surface traps [16–19].

Surface plasmon polaritons (SPPs), which emerge from a coupling between the light and collective oscillations of free electrons at a metal surface, underlie a significant number of the above-mentioned experiments. The SPPs propagate along the metal-dielectric boundary, and the amplitude of the electromagnetic field exponentially decays in both media. The nonpropagating form of SPPs, localized surface plasmons, is found in the vicinity of metallic nano-objects [20]. Both forms of SPPs have been studied with the NSOM technique [21,22]. The research includes mapping the near field associated with metallic waveguides based on stripes [23,24], nanowires [25,26], cavities [27], nanoparticles [28,29], and a gold film surface covered with randomly positioned scatterers [30,31].

The plasmon modes were also imaged in gold nanorods [32], gratings [33–35], slits [36–38], metallic discontinuities [39], the Au-Al heterostructure [40], and nanoholes [41–43]. Apart from localized and propagating SPPs, also the standing waves of SPPs have been observed with the NSOM technique for a variety of structures [44], including a set of nanoslits [45,46].

One of the available optical methods for generating SPPs uses a chain of nanograins [47–49] or a grating coupler, which, unlike any prism-based configuration, allows us to miniaturize the system [20]. The idea is to match the momenta of the tangential component of the  $k_0$  wave vector of incident light of the TM polarization state and  $k_{SPP}$ , the wave vector of SPPs. In our case, the requirement of momentum matching stands:

$$k_{SPP} = -k_0 \sin \theta + \frac{2\pi m}{d}, \quad (1)$$

where  $\theta$  is the angle of incidence ( $\theta$  in our notation is positive),  $m = 0, 1, 2, \dots$ , and  $d$  is the grating period. Among the wide selection of various grating types, the transmission structures are of particular interest because it is possible to generate the SPPs on both glass-gold and gold-air boundaries. The latter is advantageous for cold-atom experiments and NSOM imaging. Atomic mirrors use SPPs' evanescent field to create a strong, repulsive potential for an atomic cloud [16–19], but the presence of light on the gold-air side leads to unwanted atom-photon scattering. Likewise, it would be detected by the probe, disturbing the NSOM observation of SPPs themselves.

So far, only qualitative studies of the absolute enhancement of the electromagnetic field have been presented, we believe. Here, we present a quantitative analysis of the SPP excitation on the nanofabricated transmission structure. The NSOM imaging is compared with numerical models, revealing the

<sup>\*</sup>a.sierant@uj.edu.pl

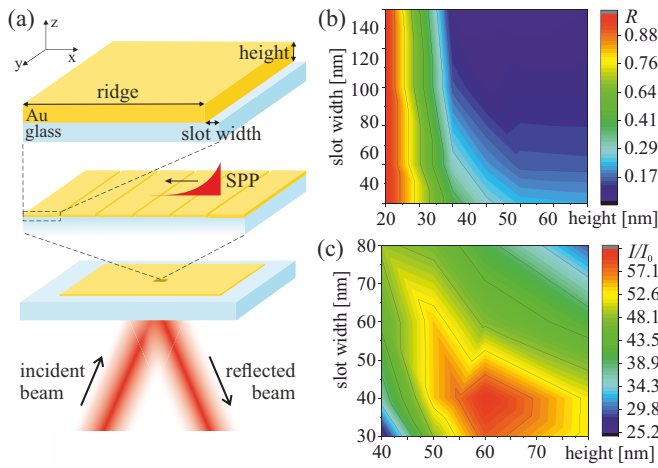


FIG. 1. Optimization of SPP excitation performed by the RCWA method. (a) Scheme of the modeled gold transmission structure, with one grating period magnified. (b) Reflectivity and (c) intensity maps for the grating of the 550 nm grating period for various slot widths and grating heights.

*in situ* processes of buildup and propagation of SPPs on a large-area grating coupler.

## II. EXPERIMENT

### A. Numerical optimization

To maximize the efficiency of the excitation process, we have numerically optimized the parameters of the grating structure, i.e., the grating period, slot width, and grating height, to obtain a narrow and deep plasmonic resonance with a strong electromagnetic field enhancement above the grating surface for near-infrared light (780 nm). We focus on narrow-width slots, as proposed by Yoon *et al.* [50]. The modeled grating geometry is presented in Fig. 1(a). We have performed in-depth calculations of the reflectivity coefficient  $R$  and electromagnetic field enhancement, given by the intensity ratio  $I/I_0$ , where  $I_0$  is the intensity of the incident light. The calculations were performed by rigorous coupled wave analysis (RCWA), using RCWA-1D, by Pavel Kwiecien from Czech Technical University in Prague. The calculations were performed in the regime of monochromatic, near-infrared 780 nm laser light, with the complex refractive index of gold equal to  $0.1478-4.6223i$  and the refractive index of glass equal to 1.51. In order to avoid light diffraction into orders other than zeroth, the scanned range of the grating periods was 400–760 nm, slot widths were 30–140 nm, and grating heights were 20–80 nm. The investigated angles of incidence were in the range of  $0^\circ-90^\circ$ . The periodic boundary conditions were implemented in the calculations, making the grating virtually an infinite structure. The most effective plasmonic resonance and electromagnetic field enhancement are obtained for the grating period equal to 550 nm with reflectivity and intensity shown in Figs. 1(b) and 1(c). The reflectivity coefficient  $R$  is minimized for slot widths of 100–140 nm and heights between 40 and 80 nm. On the other hand, taking into account the intensity of the electromagnetic field, we set the optimal range to 30–50 nm wide slots. Due to the

technically demanding fabrication process, especially in the case of large-area structures, the final parameters have been tuned so that the fabrication errors (of the order of a few nanometers) do not affect the resonance significantly. Finally, a 550 nm grating period, 55 nm grating height, and 40 nm slot width were chosen for fabrication and implemented in all calculations discussed in this paper.

### B. Fabrication

The 55 nm thick gold layer was evaporated by electron beam metal deposition onto a glass substrate, overcoated with a 3 nm titanium adhesion layer. The structure was nanofabricated by focused ion beam (FIB) milling (Dual Beam SEM/FIB Quanta 3D FEG microscope by FEI) using gallium ions with 30 keV energy in a gold layer. The grooves are 38 nm wide and 100  $\mu\text{m}$  long, continuously repeated every 550 nm, on an area of  $100 \times 100 \mu\text{m}^2$ . To prevent sample charging during FIB nanopatterning, an electron flood gun charge neutralizer was used. Directly after the FIB processing, the grating was examined with a scanning electron microscope (SEM) at 5 keV electron energy in the same apparatus. The SEM images of the grating are presented in Fig. 2(a). The detailed SEM analysis showed the presence of spherical-like grains with a diameter up to 14 nm, which was included in the numerical simulations. In total we fabricated and examined three samples of such a transmission grating (all gave similar results and will not be distinguished in this paper).

### C. Far-field investigation

Measurements of the far-field optical response of the grating were carried out using the optical setup shown in Fig. 2(d).

The collimated 780 nm laser beam (Toptica DL 100) was guided through a single-mode, polarization-maintaining fiber, followed by the polarizer (a half-wave plate and a polarization beam splitter cube), and reflected from the gold transmission grating from the glass-gold boundary. The grating was placed on a rotary stage, which allowed us to precisely change the angle of incidence. The presence of the plasmonic resonance was determined with charge-coupled device (CCD) images, taken for TE and TM polarized laser beams. The efficiency of the plasmonic coupling was determined by the reflectivity coefficient  $R$  at each angle of incidence.  $R$  was calculated as the ratio of the intensity of light at the grating to the intensity of light reflected from the plain gold (not modified by slots). The measurements were repeated for each angle separately, in a range of  $0^\circ-20^\circ$ . The position of the lens and the CCD camera were adjusted for each setting of the rotary stage.

### D. Near-field investigation

The sample was mounted in the NSOM microscope scanner (Nanonics MultiView 1000 scanning near-field microscope), and the SPPs were excited on the gold-air boundary. The optimal angle of incidence was set as a result of monitoring the intensity distribution of the reflected beam on the CCD camera. The gold-air boundary was scanned by the NSOM fiber tip to image both the electromagnetic field intensity and the surface topography. The NSOM head was integrated with an optical microscope, so that the examined area was optically

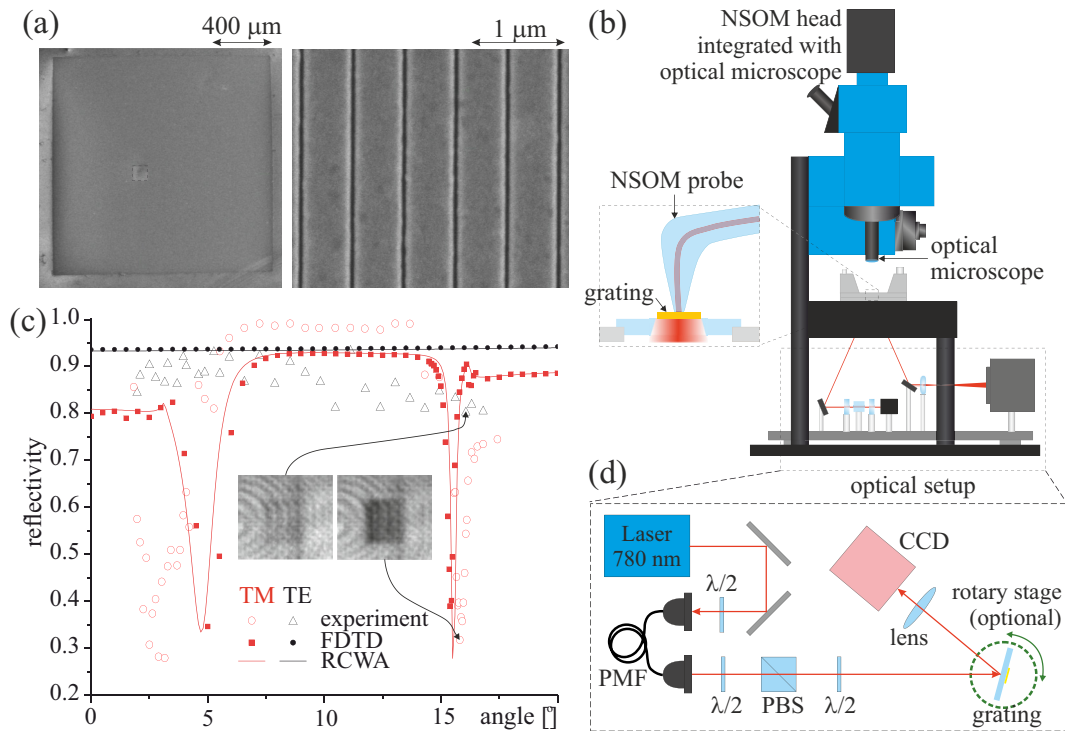


FIG. 2. (a) SEM micrographs of the transmission diffraction grating: the position of the grating on the Au/glass substrate and a detailed view of five grating periods. The grating is marked by the dashed line. (b) Schematic of the NSOM installed above the breadboard with the optical setup. (c) Angle-dependent zeroth-order reflectivity of the 780 nm laser beam: calculations performed by the finite-difference time domain (FDTD; solid circles and squares) and RCWA (solid lines) methods, compared with experiment (open circles and triangles) for TE (black) and TM (red) polarizations of light. Inset: photos of the reflected beam for the optimum angle of incidence for TE and TM polarized light, imaged by a CCD camera. (d) Scheme of the auxiliary optical setup, which was used to measure the efficiency of plasmonic resonance.  $\lambda/2$  is a half-wave plate, PBS is the polarization beam splitter, and PMF is the polarization-maintaining fiber.

observed in real time, revealing the horizontal position of the fiber tip with respect to the grating area. The NSOM was working in a collection mode, with multimode Cr-Au coated fibers of two diameters: 50 and 100 nm. Several commercially available cantilevered NSOM optical fiber probes were used, fabricated by Nanonics Imaging Ltd. (NAN.630.00199). The collected data were analyzed and compared with the surface topography registered simultaneously by the same probe (the tapping mode of an antiferromagnetic (AFM)-like operation). During the near-field measurements, the SPPs were excited with the collimated 780 nm laser beam, TM/TE polarized, at an optimal angle of incidence of  $16^\circ$ . The state of light polarization was controlled by the rotation of the half-wave plate. We have examined three samples of transmission gratings with exactly the same parameters, obtaining similar results (thus, we show typical results, and the samples will not be distinguished).

Scanning of the entire sample's area and beyond was performed with tens of measurements. A single scan size was  $20 \times 20 \mu\text{m}^2$ . For each measurement we performed finite-difference time domain (FDTD) simulations, taking into account the finite size of the grating: the modeled structure consisted of 183 grating periods surrounded by  $100 \mu\text{m}$  of plain gold on each side. The surface corrugations were included in the calculations.

The numerical simulations were performed using the FDTD method, which took into account the irregularities of

the gold surface and the *finite/infinite* size of the sample (an infinite grating is used for calculations of the Poynting flux, and a finite structure is used for near-field distribution analysis). The size and shape of the irregularities match the SEM analysis of the topography of the surface; namely, the grains are implemented as half-spheres with a diameter up to 14 nm. The grains were distributed randomly using the Wolfram *Mathematica* random number generator and cover the entire surface of the structure, both ridges and grooves. The latter corresponds to the presence of residual gold at the bottom of the groove. The near-field distributions were calculated using the FDTD method for the optimal angle of incidence, equal to  $15.4^\circ$ .

### III. RESULTS AND DISCUSSION

#### A. Far-field analysis of SPPs

In the case of far-field measurements, the presence of the SPPs is demonstrated by an extinction in the reflected light intensity, caused by the phase difference between specularly reflected and radiated light [see the inset in Fig. 2(c)]. The measured values of the  $R$  coefficient are compared with two types of numerical simulations in Fig. 2(c). The RCWA method implements the perfectly smooth, rectangular grating with periodic boundary conditions (making the modeled grating a virtually infinite structure). The FDTD method took into account the irregularities of the gold surface. The plasmonic

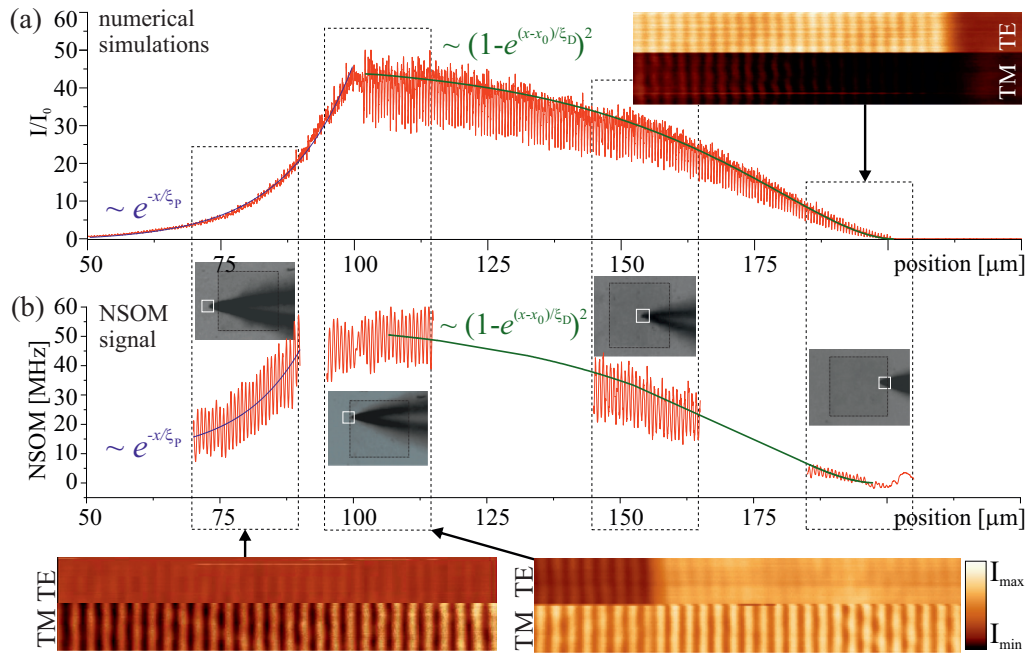


FIG. 3. Electromagnetic field enhancement above the diffraction grating (a) calculated by the FDTD method and (b) measured by NSOM. Measurements were performed in the center of the grating, on the right side, on the left side, and outside the left edge of the grating, as indicated in the graphs by images taken by the optical microscope. The grating and the scanned areas are marked with black and white squares, respectively. Also, the range of the scanned area is marked with a black dashed line in both plots. The figure is completed with NSOM images of the respective areas.  $\xi_P$  is the propagation length, and  $\xi_D$  is the buildup length.

resonances are indicated by two minima. The first minimum, located around  $4^\circ$ , results from the SPPs generated on the glass-gold boundary and is irrelevant for us due to the location of the SPPs inside the sample. The second one, located around  $16^\circ$  ( $15.4^\circ$  for simulations), corresponds to the SPPs excited on the gold-air interface with experimentally achieved reflectivity equal to 0.32 (coupling efficiency of roughly 68%) and is our area of interest. Very good agreement between the simulations performed with the RCWA and FDTD methods is observed, with some mismatch in the  $R$  coefficient calculated at the optimal angle of incidence ( $R_{RCWA} = 0.26$  and  $R_{FDTD} = 0.39$ ). The difference between  $R_{RCWA}$  and  $R_{FDTD}$  quantifies the degree to which the plasmonic resonance is deteriorated by the surface imperfections. The periodic boundary conditions imposed in numerical calculations make the modeled grating a virtually infinite structure, which causes the discrepancies between the simulations and experimental points. The real grating consisted of  $100 \mu\text{m}$  of grating periods, surrounded by a flat gold surface (hereinafter referred to as a finite grating).

### B. Near-field analysis of SPPs

The near-field intensity enhancement  $I/I_0$  for the TM state of polarization within and outside the grating area is presented in Fig. 3(a) for FDTD simulations. The plasmonic beam illuminated the sample from the left side at the optimal angle of  $16^\circ$ . In this way we distinguish *the right edge, the center, the left edge, and outside left edge* of the grating. The numerical simulations are supplemented with the intensity of the electromagnetic field measured with NSOM in Fig. 3(b).

The particular area of the grating is shown in the images, taken by the optical microscope, and completed with an appropriate NSOM image for both states of polarization. Each NSOM image presents the results obtained for TM and TE states of polarization, changed in the middle of the single  $20 \times 20 \mu\text{m}^2$  scan by the rotation of the orientation of the polarization plane by a half-wave plate. The process of SPP buildup takes place on the right side of the grating, which is demonstrated by the very low intensity for TM polarized light and poor contrast of fringes. Going to the left, the signal and the contrast become stronger. The SPPs propagate even outside the left side of the grating, and the enhancement of the field intensity reaches a factor of 50. The results are consistent with Eq. (1), which predicts the SPPs propagate backwards with respect to the excitation beam direction. Although the sample has no grooves outside the grating, the fringes are still clearly visible—this is due to the interference between the propagating SPPs and the incident beam, which leaks through the gold layer (confirmed by numerical simulations in Fig. 4, which will be discussed later). The results of the numerical simulations match qualitatively the intensity distribution measured by NSOM. Quantitative agreement for the central region will be shown later as well. The intensity profile allows us to determine the propagation length  $\xi_P$  of SPPs excited on the structure, which describes the distance at which the intensity of SPPs decreases  $e$  times [51]. The analytically calculated propagation length for a flat, gold surface of infinite thickness is  $\xi_P^{\text{flat}} = 43 \mu\text{m}$  [51]. Apart from the always-present Ohmic losses, the leakage radiation also reduces the propagation length by approximately a factor of 2 [51,52] in the case of thin layers. This is confirmed in our numerical simulations

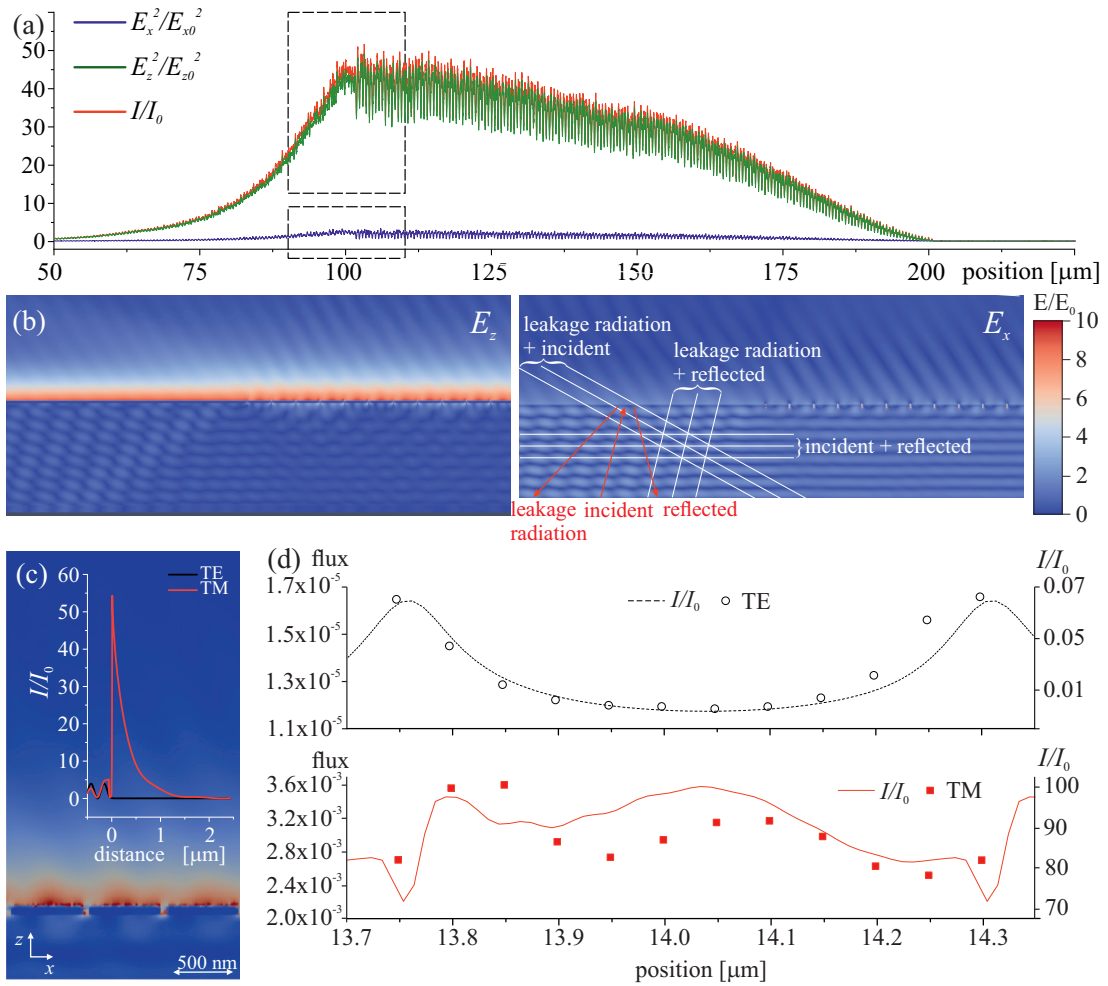


FIG. 4. FDTD simulations of the electromagnetic field enhancement above the diffraction grating. (a) A quantitative comparison between components  $E_x^2$  (in plane),  $E_z^2$  (out of plane), and total intensity  $I$  for TM polarized light. (b) Amplitude of the respective components on the left edge of the grating. The maxima of the interference pattern, resulting from interference between the incident and reflected light and leakage radiation, are schematically marked with white lines. (c) Simulated  $I/I_0$  distribution for TM (up) and TE (down) polarized light. Inset: cross section in the  $z$  direction for TE (black line) and TM (red line) polarized light. (d) Poynting flux calculated for TM (red squares) and TE (black circles) polarized light, compared with the intensity distribution calculated without the probe presence (solid lines).

for a perfectly flat gold (no irregularities on the surface), giving  $\xi_p^{\text{perf}} = 21 \mu\text{m}$ . However, to determine the propagation length in a realistic scenario, the irregularities of the grating surface must be taken into account. The exponential function  $\sim \exp(-x/\xi_p)$  has been fitted to both numerical simulations and the NSOM signal (denoted in Fig. 3 by the blue lines). The numerically calculated propagation length is  $\xi_p^{\text{FDTD}} = 12.9(0.1) \mu\text{m}$  and is consistent with the experimentally measured value  $\xi_p^{\text{EXP}} = 11.5(2.0) \mu\text{m}$ . Furthermore, the process of SPP buildup is investigated. Both numerical and experimental intensity profiles are very well described by the analytic formula [53]  $I/I_0 \sim [1 - \exp[(x - x_0)/\xi_D]]^2$ , where  $\xi_D$  is the buildup length. The calculated value of the buildup length is  $\xi_D^{\text{EXP}} = 31.0(2.0) \mu\text{m}$  for the NSOM signal, consistent with the value  $\xi_D^{\text{FDTD}} = 30.3(0.1) \mu\text{m}$  from the numerical simulations.

Before we move on to the quantitative comparison, we would like to note an important feature regarding NSOM measurements. According to Rotenberg and Kuipers, the out

of plane electric field component is greatly suppressed in NSOM detection, as opposed to the in plane component, for aperture-type probes [54]. The electric field emerging from the TM polarized light has two components:  $E_x$  and  $E_z$ , which are the in plane and out of plane components, respectively. The electric field arising due to the TE polarized light has only an  $E_y$  component, which is the in plane component detected efficiently by the NSOM probe. This means that the nature of the coupling of both polarizations to the fiber tip is in favor of the TE polarized light, whereas part of the TM signal is suppressed in the NSOM itself. A quantitative approach is shown in Figs. 4(a) and 4(b). The main plasmonic enhancement is due to the  $E_z$  component, which explains the differences between the TM/TE ratios obtained in the simulations and NSOM measurements. Results in Fig. 4(a) show that the  $E_z^2$  component (green line) is 20 times stronger than the  $E_x^2$  component (blue line), so that  $E_z^2$  almost completely overlaps with the total intensity distribution (red line). This type of relation between electric field components is an

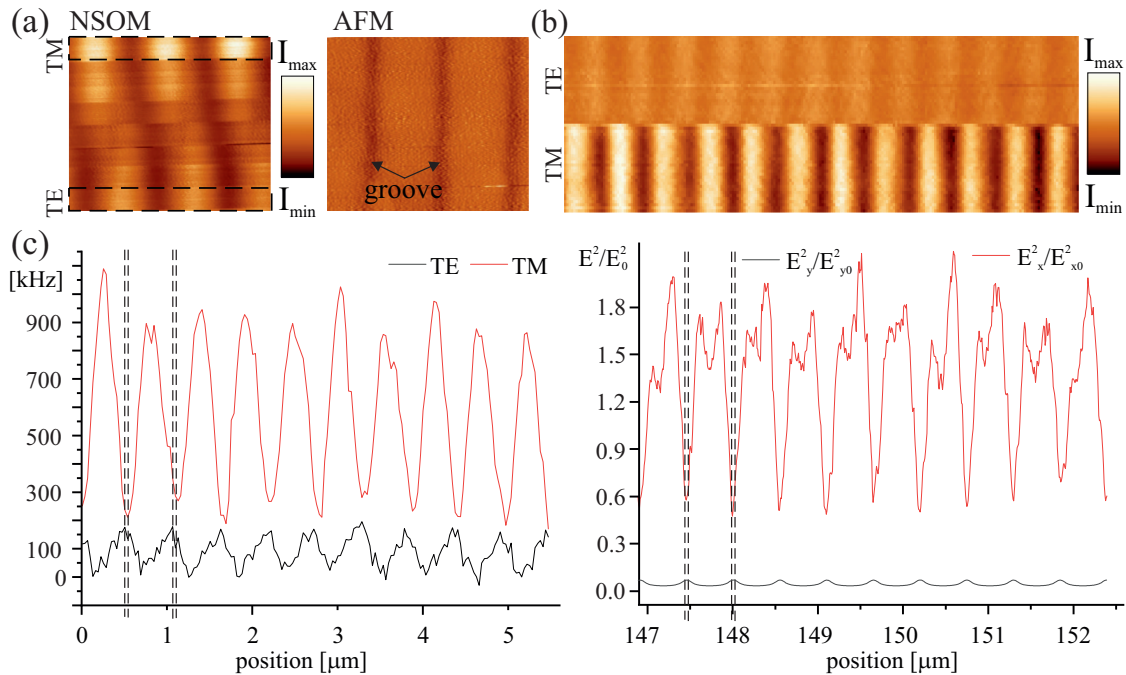


FIG. 5. Electromagnetic field enhancement above the transmission diffraction grating measured by NSOM and numerically simulated by the FDTD method for TE and TM polarized light. (a) Qualitative comparison for polarization of light varying between TE and TM, together in a single measurement cycle, with respective surface topographies. (b) Comparison between TM and TE polarizations detected by NSOM in a single measurement cycle. (c) Quantitative analysis of (b): light intensity at NSOM and FDTD cross sections, obtained for the in plane components of TM (red line) and TE (black line) polarizations of light. Two of the grating slots, based on the surface topography, are denoted by black dashed lines, given as a reference.

inherent property of SPPs on gold for the considered wavelength of 780 nm, in contrast to the case of a pure evanescent wave on a dielectric surface, where the contribution of the components may be easily varied [55]. The strong domination of the  $E_x$  component in the NSOM results explains the well-pronounced interference pattern measured outside the grating, which is hidden in simulations by the domination of the  $E_z$  component [compare Figs. 3(a) and 3(b), left side of the grating]. The interference pattern in the glass substrate volume has an interesting origin. It comes from the interference between three waves: the incident beam, the beam reflected from the gold surface, and the leakage radiation, as depicted in Fig. 4(b) (cf. [56]). The angle of incidence of the laser light is  $15.4^\circ$ , and the angle of the leakage radiation is  $43^\circ$  in glass.

The intensity distribution above three grating periods and the respective cross section are presented in Fig. 4(c). As expected, the exponential decay from the surface is revealed, thus proving the usefulness of such a structure in cold-atom experiments for the generation of an optical dipole force.

Motivated by Dvořák *et al.*, we performed the Poynting flux calculations inside the fiber probe, which take into consideration the detection of individual field components [45]. The calculation model was constructed of a  $20 \mu\text{m}$  long row of grating periods, with the NSOM probe above them (note that this is the infinite type of the structure; the calculations for the finite case were infeasible). The NSOM probe was constructed of a glass structure with a 50 nm diameter, covered with 100 nm of gold coating, and was placed 15 nm above the grating structure. After calculating the flux in one position, the simulations were repeated for the probe shifted horizontally in

50 nm increments, scanning more than one grating period in total. The summary is presented in Fig. 4(d) by comparing the value of the Poynting flux and the intensity distribution  $I/I_0$  (which was calculated without the NSOM probe but for the very same  $20 \mu\text{m}$  of grating periods and also for the infinite type of grating). The shape of the intensity distribution is reproduced for both polarization states. The TM to TE intensity ratio determined by the enhancement  $I/I_0$  equals 2000, while the one driven by the Poynting flux gives a factor of 200, reducing the no-probe ratio 10 times. This indicates that the out of plane component is not detected by NSOM, yet the shape of the distribution is accurately reproduced and can be further used.

Based on the above information, a quantitative comparison is made for the in plane components of TM and TE polarized light. Figure 5 compares the results obtained for different states of polarization, varying between TM (SPP presence) and TE (SPP absence) states, taken at the center of the grating. A qualitative demonstration is presented in Fig. 5(a), showing the signal detected by NSOM, during a change in the polarization state with the respective topography of the surface taken by NSOM. The state of polarization was varied from TM to TE polarization by rotating the orientation of the plane of polarization with a step of  $15^\circ$ . This analysis demonstrates a significant change in the intensity distribution: the maxima and minima switch positions, and the strength of the signal weakens with decreasing SPP excitation (that is, from TM to TE). The result for NSOM measurements for TM and TE polarization states is shown in Fig. 5(b). The cross sections, which allow for a quantitative comparison, are

exhibited in Fig. 5(c), together with numerical simulations of intensity enhancement for the in plane components of TM and TE polarizations. The numerical simulations were performed for the whole finite grating, but the results are presented for only 13 grating periods, taken from the middle of the grating. The positions of the minima and maxima with respect to the grating's ridges and grooves are well matched with the numerical simulations. The maxima of the TM case occur in the middle of the ridges, while the maxima of TE polarized light can be found in the vicinity of grooves. Some discrepancies can be found in the shape of the maxima, which are slightly wider in the NSOM data. This is caused by the spatial integration of the collected signal (note that the diameter of the fiber aperture is 50 nm, excluding the Cr-Au cladding, and the width of the slot is 40 nm). Furthermore, the TM case gives a stronger signal than TE, leading to a typical TM/TE ratio measured by NSOM of 10, and the highest recorded ratio was 40. According to the FDTD simulations for in plane and out of plane components, the TM/TE ratio is expected to be 30, in good agreement with the near-field measurements.

#### IV. CONCLUSION

We have used a NSOM technique to investigate the nature of SPPs on a nanofabricated transmission grating. We have optimized the parameters of the grating, and we have fabricated the structure with a FIB microscope. Our far-field goniometric measurements revealed the narrow and deep plasmonic resonance with an efficiency coupling of 68% and electromagnetic field enhancement of 50. This makes the grating an effective scientific tool for plasmonic sensing and a promising base for cold-atom experiments, including precise micropotentials tailored with subwavelength resolution through SPP excitation. The proposed transmission structure allows for the miniaturization of the system and ensures

the separation between the exciting beam from the proper part of the experiment; thus, it can be successfully used in optical dipole mirrors, surface traps, and other plasmonic devices [16,17]. We have directly observed *in situ* processes of SPPs building up with a SPP decay length of  $\xi_D^{\text{EXP}} = 31 \mu\text{m}$  and propagation outside the grating structure, with the propagation length equal to  $\xi_P^{\text{EXP}} = 11.5 \mu\text{m}$ . We have confirmed that the aperture-type probe does not couple the out of plane component of the electric field. We have also quantitatively compared the signals detected by NSOM and FDTD calculations. We have measured the intensity distribution associated with propagation of SPPs and demonstrated an accurate agreement of numerical simulations with experimental data. Our simulations also showed that it is crucial to take into account the microscopic details of the structure such as the irregularities of the gold surface and the finite size of the grating for quantitative understanding of propagation and buildup of SPPs. This paves the way for a full quantitative understanding of SPPs needed for the design and fabrication of plasmonic sensors, plasmon-based circuits, photovoltaics, nanomanipulators, electro-optic plasmonic modulators, and atomic devices.

#### ACKNOWLEDGMENTS

The authors thank Prof. J. Rysz for lending the NSOM, his expert assistance, and useful discussions and Prof. F. Krok for the opportunity to use the SEM/FIB microscope. We also thank Dr. J. Fiutowski for preparing gold substrates, Dr. P. Dąbczyński for plasma cleaning of the grating, Dr. D. Wrana for SEM imaging, Dr. D. Bartoszek-Bober for contributions to the early stage of the experiment, and Dr. P. Sierant and P. Sowa for remarks on the manuscript. We acknowledge the support of the National Science Centre of Poland (doctoral scholarship, A.S.) under Project No. 2018/28/T/ST2/00275.

- 
- [1] D. W. Pohl, W. Denk, and M. Lanz, *Appl. Phys. Lett.* **44**, 651 (1984).
  - [2] U. Dürig, D. W. Pohl, and F. Rohner, *J. Appl. Phys.* **59**, 3318 (1986).
  - [3] E. Betzig, M. Isaacson, and A. Lewis, *Appl. Phys. Lett.* **51**, 2088 (1987).
  - [4] G. Gay, O. Alloschery, B. V. De Lesegno, C. O'Dwyer, J. Weiner, and H. Lezec, *Nat. Phys.* **2**, 262 (2006).
  - [5] S. I. Bozhevolnyi, V. S. Volkov, T. Søndergaard, A. Boltasseva, P. I. Borel, and M. Kristensen, *Phys. Rev. B* **66**, 235204 (2002).
  - [6] J. Dorfmueller, D. Dregely, M. Esslinger, W. Khunsin, R. Vogelgesang, K. Kern, and H. Giessen, *Nano Lett.* **11**, 2819 (2011).
  - [7] M. Schnell, A. Garcia-Etxarri, A. Huber, K. Crozier, J. Aizpurua, and R. Hillenbrand, *Nat. Photonics* **3**, 287 (2009).
  - [8] A. Minovich, A. E. Klein, N. Janunts, T. Pertsch, D. N. Neshev, and Y. S. Kivshar, *Phys. Rev. Lett.* **107**, 116802 (2011).
  - [9] M. L. Juan, M. Righini, and R. Quidant, *Nat. Photonics* **5**, 349 (2011).
  - [10] J. F. Li, Y. F. Huang, Y. Ding, Z. L. Yang, S. B. Li, X. S. Zhou, F. R. Fan, W. Zhang, Z. Y. Zhou, D. Y. Wu, B. Ren, Z. L. Wang, and Z. Q. Tian, *Nature (London)* **464**, 392 (2010).
  - [11] A. Brolo, *Nat. Photonics* **6**, 709 (2012).
  - [12] E. Ozbay, *Science* **311**, 189 (2006).
  - [13] M. Salerno, J. R. Krenn, B. Lamprecht, G. Schider, H. Ditlbacher, N. Félidj, A. Leitner, and F. R. Aussenegg, *Opto-Electron. Rev.* **10**, 217 (2002).
  - [14] W. Cai, J. S. White, and M. L. Brongersma, *Nano Lett.* **9**, 4403 (2009).
  - [15] J. Kitching, *Appl. Phys. Rev.* **5**, 031302 (2018).
  - [16] C. Stehle, H. Bender, C. Zimmermann, D. Kern, M. Fleischer, and S. Slama, *Nat. Photonics* **5**, 494 (2011).
  - [17] M. Mildner, A. Horrer, M. Fleischer, C. Zimmermann, and S. Slama, *J. Phys. B Phys.* **51**, 135005 (2018).
  - [18] T. Kawalec, A. Sierant, R. Panaś, J. Fiutowski, D. Bartoszek-Bober, L. Józefowski, and H.-G. Rubahn, *Plasmonics* **13**, 639 (2018).
  - [19] T. Kawalec, D. Bartoszek-Bober, R. Panaś, J. Fiutowski, A. Pławecka, and H.-G. Rubahn, *Opt. Lett.* **39**, 2932 (2014).
  - [20] S. A. Maier, *Plasmonics: Fundamentals and Applications* (Springer, New York, 2007).
  - [21] W. L. Barnes, A. Dereux, and T. W. Ebbesen, *Nature (London)* **424**, 824 (2003).

- [22] B. Hecht, H. Bielefeldt, L. Novotny, Y. Inouye, and D. W. Pohl, *Phys. Rev. Lett.* **77**, 1889 (1996).
- [23] J.-C. Weeber, J. R. Krenn, A. Dereux, B. Lamprecht, Y. Lacroute, and J.-P. Goudonnet, *Phys. Rev. B* **64**, 045411 (2001).
- [24] R. Dallapiccola, C. Dubois, A. Gopinath, F. Stellacci, and L. Dal Negro, *Appl. Phys. Lett.* **94**, 243118 (2009).
- [25] J. R. Krenn, B. Lamprecht, H. Ditlbacher, G. Schider, M. Salerno, A. Leitner, and F. R. Aussenegg, *Europhys. Lett.* **60**, 663 (2002).
- [26] M. M. Wiecha, S. Al-Daffaie, A. Bogdanov, M. D. Thomson, O. Yilmazoglu, F. Kupperts, A. Soltani, and H. G. Roskos, *ACS Omega* **4**, 21962 (2019).
- [27] S. Balcı, E. Karademir, C. Kocabas, and A. Aydinli, *Opt. Lett.* **36**, 3401 (2011).
- [28] J. R. Krenn, A. Dereux, J.-C. Weeber, E. Bourillot, Y. Lacroute, J.-P. Goudonnet, G. Schider, W. Gotschy, A. Leitner, F. R. Aussenegg, and C. Girard, *Phys. Rev. Lett.* **82**, 2590 (1999).
- [29] S. A. Maier, P. G. Kik, H. A. Atwater, S. Meltzer, E. Harel, B. E. Koel, and A. A. Requicha, *Nat. Mater.* **2**, 229 (2003).
- [30] S. I. Bozhevolnyi, V. S. Volkov, and K. Leosson, *Phys. Rev. Lett.* **89**, 186801 (2002).
- [31] S. I. Bozhevolnyi, V. S. Volkov, A. Boltasseva, and K. Leosson, *Opt. Commun.* **223**, 25 (2003).
- [32] K. Imura, T. Nagahara, and H. Okamoto, *J. Chem. Phys.* **122**, 154701 (2005).
- [33] J. Jose, F. B. Segerink, J. P. Kortnerik, A. Gomez-Casado, J. Huskens, J. L. Herek, and H. L. Offerhaus, *J. Appl. Phys.* **109**, 064906 (2011).
- [34] T. Iqbal, *Curr. Appl. Phys.* **15**, 1445 (2015).
- [35] M. N. Gadalla, K. Chaudhary, C. M. Zgrabik, F. Capasso, and E. L. Hu, *Opt. Express* **28**, 14536 (2020).
- [36] H. Kihm, K. G. Lee, D. Kim, J. Kang, and Q.-H. Park, *Appl. Phys. Lett.* **92**, 051115 (2008).
- [37] P. K. Venuthurumilli, X. Wen, V. Iyer, Y. P. Chen, and X. Xu, *ACS Photonics* **6**, 2492 (2019).
- [38] D. Costantini, L. Greusard, A. Bousseksou, R. Rungsawang, T. Zhang, S. Callard, J. Decobert, F. Lelarge, G.-H. Duan, Y. De Wilde, and R. Colombelli, *Nano Lett.* **12**, 4693 (2012).
- [39] L. Salomon, G. Bassou, H. Aourag, J. P. Dufour, F. De Fornel, F. Carcenac, and A. V. Zayats, *Phys. Rev. B* **65**, 125409 (2002).
- [40] T. Kitazawa, S. Miyanishi, Y. Murakami, K. Kojima, and A. Takahashi, *Chin. Phys. Lett.* **24**, 2827 (2007).
- [41] L. Yin, V. Vlasko-Vlasov, A. Rydh, J. Pearson, U. Welp, S.-H. Chang, S. Gray, G. C. Schatz, D. Brown, and C. W. Kimball, *Appl. Phys. Lett.* **85**, 467 (2004).
- [42] R. He, X. Zhou, Y. Fu, and Y. Zhang, *Plasmonics* **6**, 171 (2011).
- [43] S.-H. Chang, S. K. Gray, and G. C. Schatz, *Opt. Express* **13**, 3150 (2005).
- [44] F. Ye, J. M. Merlo, M. J. Burns, and M. J. Naughton, *Nanophotonics* **3**, 33 (2014).
- [45] P. Dvořák, T. Neuman, L. Břínek, T. Šamořil, R. Kalousek, P. Dub, P. Varga, and T. Šikola, *Nano Lett.* **13**, 2558 (2013).
- [46] P. Dvořák, Z. Édes, M. Kvapil, T. Šamořil, F. Ligmajer, M. Hrtoň, R. Kalousek, V. Křápek, P. Dub, J. Spousta, P. Varga, and T. Šikola, *Opt. Express* **25**, 16560 (2017).
- [47] R. Frank, *Phys. Rev. B* **85**, 195463 (2012).
- [48] R. Frank, *Ann. Phys. (Berlin, Ger.)* **525**, 66 (2013).
- [49] A. Lubatsch and R. Frank, *Appl. Sci.* **10**, 1836 (2020).
- [50] K. H. Yoon, M. L. Shuler, and S. J. Kim, *Opt. Express* **14**, 4842 (2006).
- [51] H. Raether, in *Surface Plasmons on Smooth and Rough Surfaces and on Gratings* (Springer, Berlin, 1988), pp. 4–39.
- [52] K. Kolwas and A. Derkachova, *Nanomaterials* **10**, 1411 (2020).
- [53] S. T. Koev, A. Agrawal, H. J. Lezec, and V. A. Aksyuk, *Plasmonics* **7**, 269 (2012).
- [54] N. Rotenberg and L. Kuipers, *Nat. Photonics* **8**, 919 (2014).
- [55] L. Józefowski, J. Fiutowski, T. Kawalec, and H.-G. Rubahn, *J. Opt. Soc. Am. B* **24**, 624 (2007).
- [56] O. Kostiučenko, J. Fiutowski, T. Kawalec, V. Bordo, H.-G. Rubahn, and L. Józefowski, *Opt. Commun.* **331**, 77 (2014).